

Tunable directional photon scattering from a pair of superconducting qubits

Elena S. Redchenko,^{1,*} Alexander V. Poshakinskiy,² Riya Sett,¹
Martin Zemlicka,¹ Alexander N. Poddubny,² and Johannes M. Fink^{1,†}

¹*Institute of Science and Technology Austria, 3400 Klosterneuburg, Austria*

²*Ioffe Institute, St. Petersburg 194021, Russia*

(Dated: May 9, 2022)

The ability to control the direction of scattered light is crucial to provide the flexibility and scalability for a wide range of on-chip applications, such as integrated photonics, quantum information processing and nonlinear optics. In the optical and microwave frequency ranges tunable directionality can be achieved by applying external magnetic fields that modify optical selection rules [1, 2], by using nonlinear effects [3], or interactions with vibrations [4–6]. However, these approaches are less suitable to control propagation of microwave photons inside integrated superconducting quantum devices [7], that is highly desirable. Here, we demonstrate on-demand tunable directional scattering based on two periodically modulated transmon qubits coupled to a transmission line at a fixed distance [8–10] in close analogy to two oscillating mirrors [11, 12]. By continuously changing the relative phase between the local modulation tones, we realize unidirectional forward or backward photon scattering. Such an in-situ switchable mirror represents a versatile tool for intra- and inter-chip microwave photonic processors. In the future, a lattice of qubits can be used to realize topological circuits that exhibit stronger nonreciprocity or chirality [13].

One of the simplest ways to realize directional light scattering relies on the Kerker effect [14, 15]. It is based on the interference between different multipole components of scattered light, for example electric and magnetic dipoles, and has been demonstrated for Si nanoparticles [16–18]. However, the nanoparticle scattering pattern is fixed after fabrication and dictated by its shape. Tunable light routing is typically enabled by an external magnetic field that leads to the Zeeman splitting of optical transitions for clockwise- and counter-clockwise-propagating photons [1] or a modification of optical selection rules [2]. In the optical domain, the routing can be reversed as well without changing the magnetic field by flipping the spin of the atom [19]. Such structures are now actively studied in the domain of chiral quantum optics [20, 21]. Tunable directional scattering can also be achieved by using moving boundary conditions [11, 22]. For example, the trembling of a small particle with only an electric dipole resonance can induce a magnetic dipole resonance [11], which in turn provides directional scattering in analogy to the Kerker effect. Several compact nonmagnetic realizations of nonreciprocal devices using Raman and Brillouin scattering [4, 6, 23, 24] have been presented for optical frequencies.

Tunable directional interactions are also highly desired for superconducting quantum circuits in the microwave spectral range. For instance, isolators and circulators are commonly used for superconducting quantum computing to protect fragile qubits states. Cascaded photon processing in the chiral setup is also beneficial for the creation of complex entangled quantum states of qubits [25]. However, it is difficult to directly extend existing approaches for visible light to microwave photons. For ex-

ample the classical Kerker approach is not applicable to a typical transmon qubit that behaves just as an electric dipole [8], without magnetic dipole resonances. Devices, based on an external magnetic field, [26] are often bulky and always require additional shielding to protect superconducting qubits. While there exist demonstrations of directionality in parametrically driven, compact mechanical systems [27–29], integration with superconducting circuitry is challenging due to limited bandwidth and tunability. Thus, there is a need for flexible to use on-chip microwave photon routers which do not require strong magnetic fields or moving mechanical parts.

Here, our goal is to demonstrate an easy-to-fabricate circuit providing frequency and directionality tunable photon scattering with the minimum number of components required. Our approach is based on the sinusoidal time-modulation of the qubit frequency [30–32], which is a standard technique in circuit and waveguide QED. The modulated qubit strongly coupled to a waveguide can be mapped onto the problem of light scattering from the trembling mirror [11, 33]. By altering the relative phase α between the modulation tones of two qubits, we change the effective phase shift between the scattered sidebands resulting in different interference patterns for forward and backward scattering as schematically shown in Fig. 1a. Here we do not focus on the elastic scattering nonreciprocity [30, 31] or directional emission from the initial qubit state [34, 35] but on the switching between forward and backward inelastic coherent scattering. Thus, although elastically (Rayleigh) scattered radiation remains almost unaffected, we gain the flexibility to choose the frequency of the scattered photons.

* elena.redchenko@ist.ac.at

† jfink@ist.ac.at

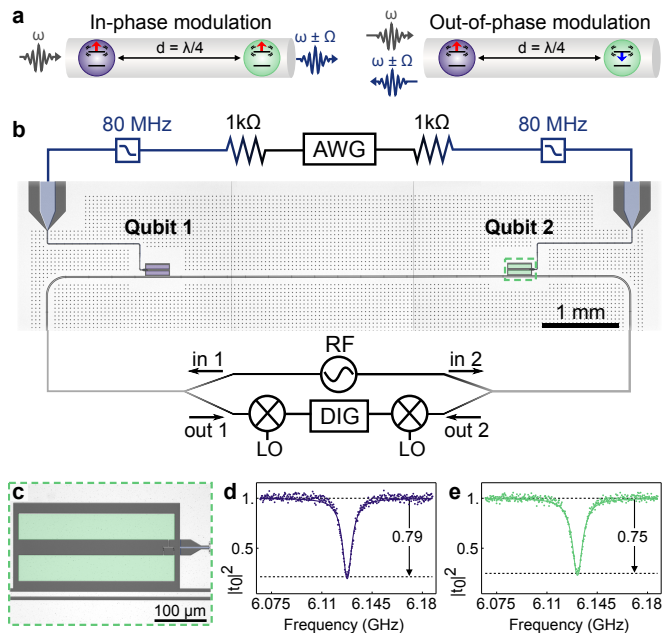


FIG. 1. **Experimental realization.** **a**, Schematic showing the scattering direction of the $\omega \pm \Omega$ component for in-phase (up-up) and out-of-phase (up-down) modulation of the qubits' transition frequencies ω . **b**, Optical microscope image and simplified experimental setup. Two transmon qubits are capacitively coupled to a 50Ω transmission line, and each qubit has a local flux bias line connected to an arbitrary waveform generator channel (AWG), which is used to generate a sinusoidal wave with an amplitude A_V that is filtered with a 80 MHz low pass filter and applied to ground via a 1 k Ω resistor. We use an RF source, analog downconversion and digitization (DIG) to back out the scattering parameters of the device cooled to 10 mK. **c**, Enlarged view of Qubit 2 and local flux bias line inductively coupled to the qubit SQUID. **d** (**e**), Individually measured and normalized transmission spectra $|t_0|^2$ of elastically scattered radiation from Qubit 1(2) with fit to theory (solid line).

EXPERIMENTAL IMPLEMENTATION

We fabricate the sample with two transmon qubits coupled to a 1D coplanar transmission line separated by $d = 5 \text{ mm}$ as shown in Fig. 1b. The maximum frequency of the $|0\rangle \rightarrow |1\rangle$ transition is 9.129 (9.577) GHz for Qubit 1(2). We tune both qubits to $\omega_0/(2\pi) = 6.129$ GHz corresponding to an effective distance of $d = \lambda/4$, with λ the wavelength of photons at ω_0 , using bias coils mounted on top of the sample box. Currents for the periodic frequency modulation are applied via on-chip bias lines inductively coupled to the SQUID loops as shown in Fig. 1c. Both ports of the transmission line are connected to separate microwave in- and output lines to measure reflection and transmission spectra simultaneously.

Firstly, we characterize the qubits individually at ω_0 where $d = \lambda/4$ using a weak resonant probe tone and measuring the coherently and elastically scattered radiation, i.e. at the same frequency. We determine the

normalized transmission spectrum of each qubit shown in Fig. 1d(e) and find the radiative decay rates to be $\Gamma_1/(2\pi) \approx 4.4$ MHz with the dephasing rates of $\Gamma_2/(2\pi) \approx 3.9$ (4.3) MHz for Qubit 1 (2) which is dominated by flux noise due to the relatively high flux dispersion at this bias point.

An applied sinusoidal bias current makes the qubit resonance frequency tremble in time and the coherent transmission amplitude is then given by

$$t_0 = 1 + \sum_{n=-\infty}^{\infty} \frac{i\Gamma_1/2}{\omega_0 + n\Omega - \omega - i\Gamma_2} J_n^2\left(\frac{A_m}{\Omega}\right), \quad (1)$$

where $J_n\left(\frac{A_m}{\Omega}\right)$ are Bessel functions of the first kind, A_m is the modulation amplitude in frequency units, and Ω is the modulation frequency. We measure the normalized transmission spectrum $|t_0|^2$ as a function of modulation frequency Ω as shown in Fig. 2a. For the fixed signal amplitude at the AWG output $A_V = 50 \text{ mV}_{\text{pp}}$, the system undergoes a transition from the strong ($A_m/2 > \Omega$) to the weak ($A_m/2 < \Omega$) modulation regime. We fit similarly measured data to Eq. 1 for both qubits individually, as shown in Fig. 2b for different applied A_V and $\Omega/(2\pi) = 20$ MHz and find that the fitted A_m scales approximately linearly with A_V , which is shown in the Supplementary Information.

MODULATED MOLLOW RESONANCE FLUORESCENCE

One of the hallmark characteristics of quantum two-level systems is the observation of the incoherent resonance fluorescence spectrum taking the form of a Mollow triplet for an applied resonant drive of sufficient power $\Omega_R > \Gamma_1$ [8]. Here we observe this effect for a frequency modulated qubit with $A_m = 0.2\Omega_R$ and Rabi frequency $\Omega_R/(2\pi) = 52$ MHz. The measured power spectral density (PSD) as a function of the modulation frequency Ω is shown in Fig. 2c and the corresponding theory in Fig. 2d. Dressing with the drive leads to the well known emission spectrum with three maxima at ω_0 and $\omega_0 \pm \Omega_R$. However, the additional frequency modulation leads to the formation of avoided crossings at $\Omega = \Omega_R$, which can be qualitatively interpreted as a formation of nested Mollow triplets following the level scheme shown in Fig. 2e. Specifically, each of the levels of the original Mollow triplet is split into two levels due to the modulation. Next, the photon transitions between the split levels lead to the formation of additional Mollow triplets. For example, the transition from the original triplet having the largest energy, and shown by the thick vertical blue arrow, is transformed by the modulation into three distinct transition energies shown by the thin blue lines. The observed splitting between the outermost transitions of the inner Mollow triplets for $\Omega = \Omega_R$ is equal to $\Delta\omega/(2\pi) \approx 20$ MHz, in excellent agreement

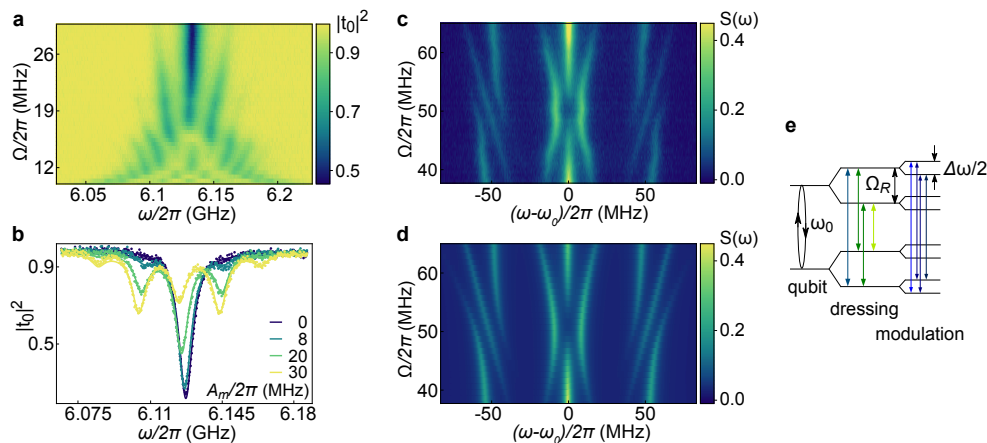


FIG. 2. **Single qubit properties.** **a**, Normalized transmission spectrum $|t_0|^2$ of qubit 1 measured as a function of the modulation frequency Ω and the probe frequency ω at the fixed modulation amplitude $A_V = 50 \text{ mV}_{\text{pp}}$. **b**, Measured $|t_0|^2$ of the modulated qubit with $\Omega/(2\pi) = 20 \text{ MHz}$ for different A_m and fits to Eq. 1 (solid lines). **c**, Measured resonance fluorescence emission spectrum of qubit 1 as a function of the modulation frequency Ω and detuning of the detected inelastically scattered radiation from the drive applied at ω_0 for a Rabi frequency $\Omega_R/(2\pi) = 52 \text{ MHz}$ and modulation amplitude $A_m = 0.2 \Omega_R$. **d**, Theoretically predicted Mollow spectrum in the presence of frequency modulation for the same parameters. **e**, Level splitting schematics of the dressed and modulated qubit, which explains the origin of the observed nested Mollow triplets at $\Omega = \Omega_R$.

with the numerical calculation.

Similar formations of nested Mollow triplets in the electron spin-noise spectrum have been predicted for the conditions of electron paramagnetic resonance when the electron is subject to a the time-modulated magnetic field [36], but have so far not been observed directly to the best of our knowledge.

DIRECTIONAL SCATTERING

Now we consider the system of two qubits both tuned to ω_0 and located at a distance $\lambda/4$. For any odd multiple of $\lambda/4$ a single resonant microwave tone drives the two qubits with opposite phase, which leads to a coherent exchange interaction mediated by virtual photons [9] forming a coupled two-qubit molecule [10]. In the absence of modulation the backscattering is suppressed by destructive interference [25], while the interference for forward scattering is constructive. The addition of frequency modulation of both qubits with $\Omega/(2\pi) = 20 \text{ MHz}$ and $A_m/(2\pi) = 20 \text{ MHz}$ results in nontrivial interference conditions for the Stokes and anti-Stokes side-bands, as shown in the insets of Fig. 3. The blue and green arrows correspond to the incident light (dashed) and the inelastically scattered light (solid) at $\pm 20 \text{ MHz}$ from the first and second qubit, respectively. If the two modulation tones are in phase ($\alpha = 0$), illustrated in the insets of Fig. 3a and c by red arrows inside the qubits (up-up), the device continues to scatter light only in the forward direction since its symmetry is not modified by the modulation. Accordingly, we observe side-bands mostly scattered forward and almost fully suppressed in back scattering (dashed circles in panels a and c). However, if

the modulation has a phase difference of $\alpha = \pi$, the situation is reversed. This is illustrated by the blue arrows inside the second qubit (up-down) in the insets of Fig. 3b and d, corresponding to an additional phase factor of -1 . While the inelastic backscattering is now highly likely as shown in Fig. 3d, the side-bands scattered forward from the first qubit destructively interfere with the ones scattered from the second one due to the additional phase shift and thus preventing forward scattering as shown in Fig. 3b.

In order to better illustrate the phase and detuning dependence of the interference conditions we extract the coherent scattering power of the Stokes component over the full range of α and for finite detuning from the qubit resonances at ω_0 . For this measurement the detection frequency is always detuned by the chosen modulation frequency $\Omega/(2\pi) = 20 \text{ MHz}$ from the probe tone at frequency ω . Here we detect both the transmitted and reflected scattered Stokes light with the two channels of the digitizer simultaneously for $A_m/(2\pi) = 30 \text{ MHz}$. The obtained intensity in transmission and reflection is shown in Fig. 4a and b. We observe resonances at probe frequencies ω_0 , $\omega_0 \pm \Omega$, and $\omega_0 - 2\Omega$ and their overall dependence on α is clearly pronounced and opposite in sign for forward and backward scattering. These experimental results are in very good agreement with the theoretical model shown in Fig. 4(b,d), see Methods for details.

The measured dependence of the scattering parameters on the phase difference α as well as the directivity $D = (P_{\rightarrow} - P_{\leftarrow})/(P_{\rightarrow} + P_{\leftarrow})$ is shown in Fig. 4e for $(\omega - \omega_0)/(2\pi) = \Omega/(2\pi) = -20 \text{ MHz}$ (dashed white lines in panels a-d) together with theory. This shows phase selective control to enter the regimes when light is mostly scattered back ($D < 0$), forward ($D > 0$), or symmetric

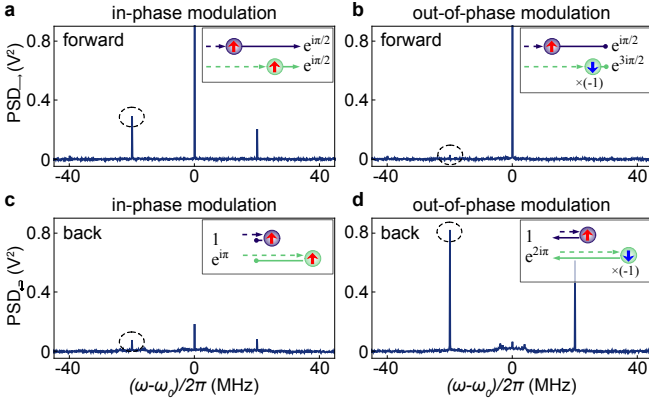


FIG. 3. **Resonance fluorescence spectra.** Power spectral density (PSD) measured in transmission (a, b) and reflection (c, d) at the digitizer for in-phase $\alpha = 0$ (a, c) and out-of-phase $\alpha = \pi$ (b, d) modulation. The Stokes components are highlighted with dashed circles. Scattering schematics are shown as insets where blue (green) arrows represent the light scattered from qubit 1 (2) at $\omega_0 \pm \Omega$ leading to constructive interference in a and d or destructive interference in b and c. Full Rayleigh peak heights are 1.9 and 1.6 V^2 for the chosen settings in a and b.

cally in both directions ($D = 0$). The measured directivity demonstrates high diode efficiency that can be set continuously between 0.84 and -0.99.

DISCUSSION

Besides the demonstrated high scattering directionality, at the relative phase $\alpha/\pi = \pm 1$, our system exhibits a gyrator-like behavior and transmits a signal unchanged in one direction whereas the reverse traveling signal experiences a π phase-shift. For $\alpha/\pi = \pm 0.3$, our device demonstrates isolator properties, which might be enhanced by further tuning the device or by extending the principle to a larger number of qubits, details can be found in the Supplementary Discussion. This nonreciprocity relies on the qubits working in the linear regime, which would naturally limit the operation of the device to low powers $(\Omega_R/\Gamma_1)^2 \ll 1$. In contrast, our calculations indicate that scattering remains directional up to intermediate drive powers $(\Omega_R/\Gamma_1)^2 \lesssim 9$ beyond which the inelastic scattering is fully suppressed, see Supplementary Figures.

We have demonstrated an on-chip microwave photon router that can be switched *in-situ* between scattering photons back, forward, or symmetrically in both directions. While it is limited in dynamic range, it is fully compatible with modern superconducting quantum computing devices [7, 34] that operate in the single and few photon regime. The suppression strength can be modified by the modulation amplitude and the signal frequency can be shifted and fine-tuned *in-situ* by changing

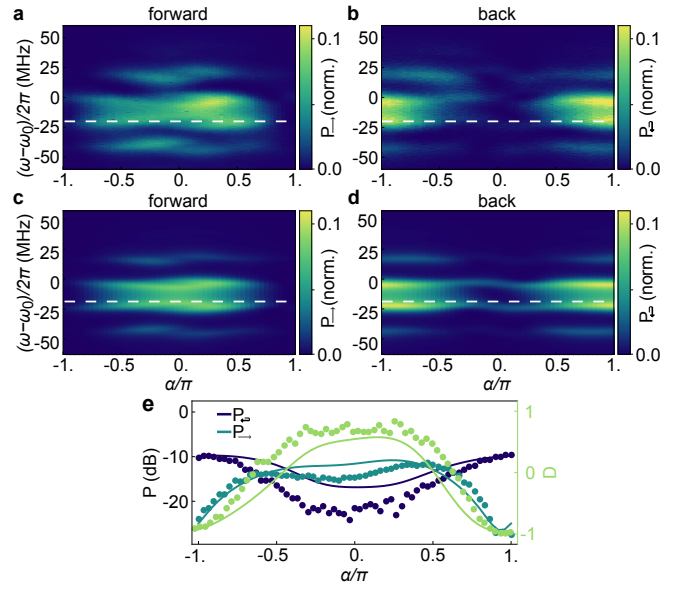


FIG. 4. **Coherent inelastic scattering spectrum of the Stokes component.** a(b), Measured and normalized Stokes power as a function of probe frequency detuning $\omega - \omega_0$ and relative phase between modulation tones α measured in transmission (reflection) at a fixed modulation amplitude $A_m/(2\pi) = 30$ MHz and modulation frequency $\Omega/(2\pi) = 20$ MHz. c(d), Theoretically predicted transmission (reflection) spectrum on the same scale. e, Measured coherent inelastic scattering as a function of α at $(\omega - \omega_0)/(2\pi) = \Omega/(2\pi) = -20$ MHz (points) and theory (solid lines). Scattering directivity D is shown in light green.

the modulation frequency. A larger range of frequency bands can be accessed by working at odd multiples of the $\lambda/4$ boundary condition. In the future, this device principle could be extended to multiple nodes, see Methods and Supplementary Information, in order to realize topologically protected states [37], as a part of a hardware implementation of Gottesman-Kitaev-Preskill codes [38], or to route microwave radiation for the realization of chiral networks [20].

METHODS

Calculation of scattering spectra. In this section we present the general approach to calculate photon scattering from an array of qubits with time-modulated resonance frequencies. Such a device is characterized by the following effective non-Hermitian Hamiltonian [39]:

$$H(t) = \sum_j [\omega_0^{(j)}(t) - i\Gamma_2^{(j)}] \sigma_j^\dagger \sigma_j - \frac{i\Gamma_1}{2} \sum_{j,k} e^{i\varphi|j-k|} \sigma_j^\dagger \sigma_k + \frac{\Omega_R}{2} \sum_j (\sigma_j^\dagger e^{i\varphi j - i\omega t} + \text{H.c.}). \quad (2)$$

Here σ_j are the raising operators, Γ_1 is the (radiative) relaxation rate between the $|1\rangle$ and $|0\rangle$ qubit states, $\Gamma_2^{(j)}$ is the decay rate of the coherence between the $|1\rangle$ and $|0\rangle$ states, $\varphi = \omega_0 d/c$ is the

phase gained by light traveling between the qubits with propagation velocity c . The Rabi frequency Ω_R quantifies the incident wave amplitude and

$$\omega_0^{(j)}(t) = \omega_0 + A_m \cos(\Omega t + \alpha_j) \quad (3)$$

are the time-dependent qubit resonance frequencies. The Hamiltonian Eq. (2) assumes the usual rotating wave and Markovian approximations. Here, we are interested in the case of weak coherent driving where the wavefunction can be approximately written as

$$\psi = |0\rangle + \sum_j p_j \sigma_j^\dagger |0\rangle. \quad (4)$$

The amplitudes p_j describe the coherence between the ground and excited states and can be found from the following Schrödinger equation:

$$i \frac{d}{dt} p_j(t) = [\omega_0^{(j)}(t) - i\Gamma_2^{(j)}] p_j - \frac{i\Gamma_1}{2} \sum_k e^{i\varphi|j-k|} p_k + \frac{\Omega_R}{2} e^{i\varphi j - i\omega t}. \quad (5)$$

It is convenient to seek the solution in the form

$$p_j(t) = \sum_{n=-\infty}^{\infty} p_j^{(n)} e^{-i(\omega+n\Omega)t}, \quad (6)$$

so that the amplitudes $p_j^{(n)}$ are determined by the linear system [40]

$$(\omega + n\Omega) p_j^{(n)} = (\omega_0 - i\Gamma_2^{(j)}) p_j^{(n)} + \frac{A_m}{2} (e^{i\alpha_j} p_j^{(n-1)} + e^{i\alpha_j} p_j^{(n+1)}) - \frac{i\Gamma_1}{2} \sum_k e^{i\varphi|j-k|} p_k^{(n)} + \frac{\Omega_R}{2} e^{i\varphi j} \delta_{m,0}. \quad (7)$$

After the amplitudes $p_j^{(n)}$ have been found numerically, we calculate the coefficients $r^{(n)}$ and $t^{(n)}$

$$r^{(n)} = -\frac{i\Gamma_1}{\Omega_R} \sum_j e^{i\varphi j} p_j^{(n)}, \quad (8)$$

$$t^{(n)} = \delta_{n,0} - \frac{i\Gamma_1}{\Omega_R} \sum_j e^{-i\varphi j} p_j^{(n)}, \quad (9)$$

that describe the backward (forward) scattering process with the frequency change $\omega \rightarrow \omega + n\Omega$. In the general case, the system of equations (7) is to be solved numerically. However, it is possible to obtain an analytical solution in the particular case of a single qubit [41]. In this case we find

$$p^{(n)} = \frac{\Omega_R}{2} \sum_{n'=-\infty}^{\infty} \frac{J_{n'-n}(A_m/\Omega) J_{n'}(A_m/\Omega)}{\omega + n'\Omega - \omega_0 + i\Gamma_2}. \quad (10)$$

For elastic scattering ($n = 0$) Eq. (10) leads to Eq. (1) in the main text.

Resonance fluorescence of the time-modulated device. Here we describe the procedure to calculate the nested Mollow triplets shown in Fig. 2. The state of the qubit can be conveniently represented as vector \mathbf{S} of the spin 1/2, where $|1\rangle$ and $|0\rangle$ states correspond to $S_z = 1/2$ and $-1/2$, respectively. The dynamics $\mathbf{S}(t)$ is governed by the Bloch equation that reads

$$\frac{d\mathbf{S}}{dt} = \mathbf{S} \times \tilde{\Omega}(t) - \mathbf{\Gamma}(\mathbf{S} - \mathbf{S}_0) \quad (11)$$

where

$$\tilde{\Omega}(t) = [\Omega_R \cos \omega t, \Omega_R \sin \omega t, \omega_0 + \Delta\omega \cos(\Omega t + \alpha)] \quad (12)$$

is the time-dependent effective magnetic field, $\mathbf{S}_0 = [0, 0, -1/2]$ is the equilibrium spin, and the spin relaxation term reads $\mathbf{\Gamma}(\mathbf{S} - \mathbf{S}_0) \equiv [\Gamma_2 S_x, \Gamma_2 S_y, \Gamma_1(S_z + 1/2)]$. The emission spectrum is deter-

mined by the spin correlation function

$$I(\omega) \propto \text{Re} \int_0^\infty dt e^{-i\omega\tau} \langle\langle S_+(t+\tau) S_-(t) \rangle\rangle_t, \quad (13)$$

where $S_\pm = S_x \pm iS_y$ and the double angular brackets denote averaging over the absolute time t . Equation (13) establishes the correspondence between the emission spectrum in the considered quantum optics problem and the electron spin noise spectrum in the conditions of electron paramagnetic resonance, when the electron is subject to two magnetic fields, a constant one and an oscillating one [36].

In the theory of magnetic resonance, the standard trick to solve Eq. (11) analytically is to switch to a reference frame rotating around the z axis with the drive frequency ω . There, the spin dynamics is governed by the same Eq. (11) but $\tilde{\Omega}(t)$ shall be replaced with

$$\Omega'(t) = [\Omega_R, 0, \omega_0 - \omega + \Delta\omega \cos \Omega t]. \quad (14)$$

In the absence of modulation, $\Delta\omega = 0$, the effective magnetic field $\Omega'(t)$ would be constant and its amplitude

$$\Omega'_R = \sqrt{\Omega_R^2 + (\omega_0 - \omega)^2} \quad (15)$$

would determine the splitting in the conventional Mollow triplet.

The presence of modulation can be accounted for by repeating the trick and switching to yet another frame rotating with frequency Ω'_R with respect to the previous one. There, $\Omega'(t)$ is replaced with

$$\Omega'' = \frac{\Omega_R \Delta\omega}{2\Omega'_R{}^2} [\omega - \omega_0, 0, \Omega_R] + \left(1 - \frac{\Omega}{\Omega'_R}\right) [\Omega_R, 0, \omega_0 - \omega], \quad (16)$$

where we neglected all oscillating terms, since they average to zero. The amplitude of Ω'' determines the splitting of the nested Mollow triplet

$$\Omega''_R = \sqrt{\left(\frac{\Omega_R \Delta\omega}{2\Omega'_R}\right)^2 + (\Omega'_R - \Omega)^2}. \quad (17)$$

Returning back to the initial reference frame, we obtain nine possible emission frequencies

$$\omega_{p,q} = \omega + p\Omega'_R + q\Omega''_R, \quad (18)$$

where $p, q = 0, \pm 1$ enumerate the components of the two nested Mollow triplets. In the above analytical solution, we used the rotating wave approximation, which is valid provided $\Delta\omega \ll \Omega_R \ll \omega_0$.

Data normalization. We normalize the transmission spectra $|t_0|^2$ shown in Fig. 1d, e and Fig. 2a, b by dividing the background transmission coefficient $|t_0|^2 = |t|^2/|t_{bg}|^2$. Here, $|t_{bg}|^2$ is measured with both qubits tuned out of the frequency range of interest and $|t|^2$ is measured with the qubit tuned to the desired frequency. This method normalizes the gain in the system and compensates for the frequency-dependent transmission properties of the drive and detection lines.

The power spectral density of the measured resonance fluorescence spectrum $S(\omega)$ shown in Fig. 2c, as well as the coherent inelastic scattering spectra shown in Fig. 4a, b were scaled to the numerically predicted value. The latter relies on the qubit parameters extracted from the transmission measurements, the chosen modulation frequency and the independently calibrated modulation amplitude.

Data availability

All datasets and analysis files used in this study will be made available on the Zenodo repository before publication.

Acknowledgments

The authors thank L. Drmic and P. Zielinski for software development, and the MIBA workshop and the IST nanofabrication facility for technical support. This work was supported by the Austrian

Science Fund (FWF) through BeyondC (F7105) and IST Austria. E.R. is the recipient of a DOC fellowship of the Austrian Academy of Sciences at IST Austria. J.M.F. and M.Z. acknowledge support from the European Research Council under grant agreement No 758053 (ERC StG QUNNECT) and a NOMIS foundation research grant. The work of A.N.P. and A.V.P. has been supported by the Russian Science Foundation under the grant No 20-12-00194.

Author contributions

E.S.R. designed and fabricated the samples, worked on the setup and performed the measurements. A.V.P. and A.N.P. developed the theory and together with E.S.R. conducted the data analysis. M.Z. contributed to building the measurement setup and R.S. to the resonance fluorescence data acquisition code. E.S.R. and A.N.P. wrote the manuscript with contributions from all authors. J.M.F. supervised this work.

Competing interests

The authors declare no competing interests.

REFERENCES

- [1] I. Söllner, S. Mahmoodian, S. L. Hansen, L. Midolo, A. Javadi, G. Kiršanskė, T. Pregolato, H. El-Ella, E. H. Lee, J. D. Song, S. Stobbe, and P. Lodahl, Deterministic photon–emitter coupling in chiral photonic circuits, *Nature Nanotech* **10**, 775 (2015).
- [2] F. Spitzer, A. N. Poddubny, I. A. Akimov, V. F. Sapega, L. Klompmaker, L. E. Kreilkamp, L. V. Litvin, R. Jede, G. Karczewski, M. Wiater, T. Wojtowicz, D. R. Yakovlev, and M. Bayer, Routing the emission of a near-surface light source by a magnetic field, *Nature Physics* **14**, 1043 (2018).
- [3] A. Rosario Hamann, C. Müller, M. Jerger, M. Zanner, J. Combes, M. Pletyukhov, M. Weides, T. M. Stace, and A. Fedorov, Nonreciprocity realized with quantum nonlinearity, *Phys. Rev. Lett.* **121**, 123601 (2018).
- [4] C. G. Poulton, R. Pant, A. Byrnes, S. Fan, M. J. Steel, and B. J. Eggleton, Design for broadband on-chip isolator using stimulated Brillouin scattering in dispersion-engineered chalcogenide waveguides, *Opt. Express* **20**, 21235 (2012).
- [5] E. A. Kittlaus, N. T. Otterstrom, and P. T. Rakich, On-chip inter-modal Brillouin scattering, *Nature communications* **8**, 1 (2017).
- [6] A. H. Safavi-Naeini, D. Van Thourhout, R. Baets, and R. Van Laer, Controlling phonons and photons at the wavelength scale: integrated photonics meets integrated phononics, *Optica* **6**, 213 (2019).
- [7] K. Reuer, J.-C. Besse, L. Wernli, P. Magnard, P. Kurpiers, G. J. Norris, A. Wallraff, and C. Eichler, Realization of a universal quantum gate set for itinerant microwave photons, *Phys. Rev. X* **12**, 011008 (2022).
- [8] O. Astafiev, A. M. Zagoskin, A. Abdumalikov, Y. A. Pashkin, T. Yamamoto, K. Inomata, Y. Nakamura, and J. S. Tsai, Resonance fluorescence of a single artificial atom, *Science* **327**, 840 (2010).
- [9] A. F. van Loo, A. Fedorov, K. Lalumière, B. C. Sanders, A. Blais, and A. Wallraff, Photon-mediated interactions between distant artificial atoms, *Science* **342**, 1494 (2013).
- [10] B. Kannan, A. Almanakly, Y. Sung, A. Di Paolo, D. A. Rower, J. Braumüller, A. Melville, B. M. Niedzielski, A. Karamlou, K. Serniak, A. Vepsäläinen, M. E. Schwartz, J. L. Yoder, R. Winik, J. I.-J. Wang, T. P. Orlando, S. Gustavsson, J. A. Grover, and W. D. Oliver, On-demand directional photon emission using waveguide quantum electrodynamics, *arXiv:2203.01430* (2022).
- [11] A. Poshakinskiy and A. Poddubny, Optomechanical Kerker effect, *Physical Review X* **9**, 011008 (2019).
- [12] M. Mirhosseini, E. Kim, X. Zhang, A. Sipahigil, P. B. Dieterle, A. J. Keller, A. Asenjo-Garcia, D. E. Chang, and O. Painter, Cavity quantum electrodynamics with atom-like mirrors, *Nature* **569**, 692 (2019).
- [13] T. Ozawa, H. M. Price, A. Amo, N. Goldman, M. Hafezi, L. Lu, M. C. Rechtsman, D. Schuster, J. Simon, O. Zilberberg, and I. Carusotto, Topological photonics, *Rev. Mod. Phys.* **91**, 015006 (2019).
- [14] M. Kerker, D.-S. Wang, and C. Giles, Electromagnetic scattering by magnetic spheres, *JOSA* **73**, 765 (1983).
- [15] W. Liu and Y. S. Kivshar, Generalized Kerker effects in nanophotonics and meta-optics [invited], *Optics Express* **26**, 13085 (2018).
- [16] I. Staude, A. E. Miroschnichenko, M. Decker, N. T. Fofang, S. Liu, E. Gonzales, J. Dominguez, T. S. Luk, D. N. Neshev, I. Brener, and Y. Kivshar, Tailoring Directional Scattering through Magnetic and Electric Resonances in Subwavelength Silicon Nanodisks, *ACS Nano* **7**, 7824 (2013).
- [17] Y. H. Fu, A. I. Kuznetsov, A. E. Miroschnichenko, Y. F. Yu, and B. Luk'yanchuk, Directional visible light scattering by silicon nanoparticles, *Nature communications* **4**, 1 (2013).
- [18] S. Person, M. Jain, Z. Lapin, J. J. Sáenz, G. Wicks, and L. Novotny, Demonstration of zero optical backscattering from single nanoparticles, *Nano Letters* **13**, 1806 (2013).
- [19] M. Scheucher, A. Hilico, E. Will, J. Volz, and A. Rauschenbeutel, Quantum optical circulator controlled by a single chirally coupled atom, *Science* **354**, 1577 (2016).
- [20] P. Lodahl, S. Mahmoodian, S. Stobbe, A. Rauschenbeutel, P. Schneeweiss, J. Volz, H. Pichler, and P. Zoller, Chiral quantum optics, *Nature* **541**, 473 (2017).
- [21] A. S. Prasad, J. Hinney, S. Mahmoodian, K. Hammerer, S. Rind, P. Schneeweiss, A. S. Sørensen, J. Volz, and A. Rauschenbeutel, Correlating photons using the collective nonlinear response of atoms weakly coupled to an optical mode, *Nature Photonics* **14**, 719 (2020).
- [22] S. Zhang, Y. Hu, G. Lin, Y. Niu, K. Xia, J. Gong, and S. Gong, Thermal-motion-induced non-reciprocal quantum optical system, *Nature Photonics* **12**, 744 (2018).
- [23] J. Müller, M. Krause, H. Renner, and E. Brinkmeyer, Measurement of nonreciprocal spontaneous Raman scattering in silicon photonic wires, *Optics Express* **18**, 19532 (2010).
- [24] E. A. Kittlaus, N. T. Otterstrom, P. Kharel, S. Gertler, and P. T. Rakich, Non-reciprocal interband Brillouin modulation, *Nature Photonics* **12**, 613 (2018).
- [25] P.-O. Guimond, B. Vermersch, M. L. Juan, A. Sharafiev, G. Kirchmair, and P. Zoller, A unidirectional on-chip photonic interface for superconducting circuits, *npj Quantum Information* **6**, 32 (2020).
- [26] A. Mahoney, J. Colless, S. Pauka, J. Hornibrook, J. Watson, G. Gardner, M. Manfra, A. Doherty, and D. Reilly, On-chip microwave quantum Hall circulator, *Physical Review X* **7**, 011007 (2017).
- [27] G. A. Peterson, F. Lecocq, K. Cicak, R. W. Simmonds, J. Aumentado, and J. D. Teufel, Demonstration of efficient nonreciprocity in a microwave optomechanical circuit, *Physical Review X* **7**, 031001 (2017).
- [28] N. R. Bernier, L. D. Tóth, A. Koottandavida, M. A. Ioannou, D. Malz, A. Nunnenkamp, A. K. Feofanov, and T. J. Kippenberg, Nonreciprocal reconfigurable microwave optomechanical circuit, *Nature Communications* **8** (2017).
- [29] S. Barzanjeh, M. Wulf, M. Peruzzo, M. Kalaei, P. Dieterle, O. Painter, and J. M. Fink, Mechanical on-chip microwave circulator, *Nature communications* **8**, 1 (2017).
- [30] B. J. Chapman, E. I. Rosenthal, J. Kerckhoff, B. A. Moores, L. R. Vale, J. Mates, G. C. Hilton, K. Lalumière, A. Blais, and K. Lehnert, Widely tunable on-chip microwave circulator for superconducting quantum circuits, *Physical Review X* **7**, 041043 (2017).
- [31] E. I. Rosenthal, B. J. Chapman, A. P. Higginbotham, J. Kerckhoff, and K. W. Lehnert, Breaking Lorentz reciprocity with frequency conversion and delay, *Phys. Rev. Lett.* **119**, 147703 (2017).

- [32] M. Liu, D. A. Powell, Y. Zarate, and I. V. Shadrivov, Huygens' metadevices for parametric waves, *Phys. Rev. X* **8**, 031077 (2018).
- [33] M.-T. Jackel and S. Reynaud, Fluctuations and dissipation for a mirror in vacuum, *Quantum Optics: Journal of the European Optical Society Part B* **4**, 39 (1992).
- [34] B. Kannan, D. L. Campbell, F. Vasconcelos, R. Winik, D. K. Kim, M. Kjaergaard, P. Krantz, A. Melville, B. M. Niedzielski, J. L. Yoder, T. P. Orlando, S. Gustavsson, and W. D. Oliver, Generating spatially entangled itinerant photons with waveguide quantum electrodynamics, *Science Advances* **6**, eabb8780 (2020).
- [35] N. Gheeraert, S. Kono, and Y. Nakamura, Programmable directional emitter and receiver of itinerant microwave photons in a waveguide, *Phys. Rev. A* **102**, 053720 (2020).
- [36] A. Poshakinskiy and S. Tarasenko, Spin noise at electron paramagnetic resonance, *Physical Review B* **101**, 075403 (2020).
- [37] L. Lu, J. D. Joannopoulos, and M. Soljačić, Topological states in photonic systems, *Nature Physics* **12**, 626 (2016).
- [38] M. Rymarz, S. Bosco, A. Ciani, and D. P. DiVincenzo, Hardware-encoding grid states in a nonreciprocal superconducting circuit, *Phys. Rev. X* **11**, 011032 (2021).
- [39] T. Caneva, M. T. Manzoni, T. Shi, J. S. Douglas, J. I. Cirac, and D. E. Chang, Quantum dynamics of propagating photons with strong interactions: a generalized input–output formalism, *New Journal of Physics* **17**, 113001 (2015).
- [40] A. N. Poddubny and L. E. Golub, Ratchet effect in frequency-modulated waveguide-coupled emitter arrays, *Phys. Rev. B* **104**, 205309 (2021).
- [41] F. Marquardt, J. G. E. Harris, and S. M. Girvin, Dynamical multistability induced by radiation pressure in high-finesse micromechanical optical cavities, *Phys. Rev. Lett.* **96**, 103901 (2006).
- [42] A. Celi, P. Massignan, J. Ruseckas, N. Goldman, I. B. Spielman, G. Juzeliūnas, and M. Lewenstein, Synthetic gauge fields in synthetic dimensions, *Phys. Rev. Lett.* **112**, 043001 (2014).
- [43] L. Yuan, Y. Shi, and S. Fan, Photonic gauge potential in a system with a synthetic frequency dimension, *Opt. Lett.* **41**, 741 (2016).
- [44] K. Lalumière, B. C. Sanders, A. F. van Loo, A. Fedorov, A. Wallraff, and A. Blais, Input-output theory for waveguide QED with an ensemble of inhomogeneous atoms, *Phys. Rev. A* **88**, 043806 (2013).

Supplementary Information for: Tunable directional photon scattering from a pair of superconducting qubits

SUPPLEMENTARY DISCUSSION

Gyrator properties

At the relative phase $\alpha/\pi = \pm 1$, the scattering coefficients of inelastic transmission in different directions are equal in absolute value and have different signs, $S_{12} = -S_{21}$, (π phase-shift) which is indeed one of the signatures of a gyrator with the ideal S-matrix

$$S_{\text{gyrator}} = \begin{pmatrix} 0 & 1 \\ -1 & 0 \end{pmatrix}. \quad (19)$$

For the presented device the nonreciprocal phase shift is robust for variable system parameters as it only depends on the correct relative phase between the two modulation tones. However, at $\alpha/\pi = \pm 1$, our device mostly scatters backward, which means that $|S_{12(21)}| \ll |S_{11(22)}|$ and the gyrator efficiency is rather low.

Isolator properties

According to our theory, isolator behavior is expected at the relative phases $\alpha/\pi \approx \pm 0.3$, where the reflection in both directions is strongly suppressed and where there is an asymmetry in transmission in opposite directions resembling the S-matrix of an ideal isolator

$$S_{\text{isolator}} = \begin{pmatrix} 0 & 0 \\ 1 & 0 \end{pmatrix}. \quad (20)$$

For the measurements at a modulation frequency $\Omega/(2\pi) = 20$ MHz and modulation amplitude $A_m/(2\pi) = 30$ MHz, we find an isolation of $10 \log_{10}(S_{21}/S_{12}) \sim 3.3$ dB and an insertion loss of $10 \log_{10} S_{21} \sim 11$ dB at $\alpha/\pi \approx -0.3$ as shown in Fig. 5.

While the insertion losses cannot be fully avoided both parameters could be improved with an increase of the modulation amplitude. Moreover, adding more qubits to the device while keeping the effective distance between nearest neighbors at $\lambda/4$ and the relative phase $\alpha/\pi = 0.5$ between modulation tones would enable the creation of a topological isolator for both elastically and inelastically scattered light [40, 42, 43].

Power dependence of directionality

In this section we discuss the dependence of the directionality on the incident wave power. In order to calculate the scattering we use the master equation [44] for the density matrix ρ :

$$\dot{\rho} = -i[H_1, \rho] + \sum_{j,k=1}^N \left(\frac{\Gamma_1}{2} \cos[\varphi(j-k) + \Gamma_2 \delta_{j,k}] \left[2\sigma_j \rho \sigma_k^\dagger - \{\sigma_k^\dagger \sigma_j, \rho\} \right] \right) \quad (21)$$

with the Hamiltonian

$$H_1 = \sum_{j=1}^N [\omega_0 + A_m(t) \cos(\Omega t + \alpha_j)] \sigma_j^\dagger \sigma_j + \frac{\Gamma_1}{2} \sum_{j,k=1}^N \sigma_j^\dagger \sigma_k \sin(\varphi|j-k|) + \sum_{j=1}^N \frac{\Omega_R}{2} (e^{-i\varphi j - i(\omega - \omega_0)t} \sigma_j^\dagger + \text{H.c.}). \quad (22)$$

The coherent reflection and transmission coefficients that describe the backward (forward) scattering process with the frequency change $\omega \rightarrow \omega + n\Omega$ are then found as the Fourier transforms

$$r_n = \frac{2}{\Omega_R} \lim_{T \rightarrow \infty} \frac{1}{T} \int_0^T dt e^{-i(\omega+n\Omega)t} \sum_{j=1}^N [\text{Tr} \rho(t) \sigma_j^\dagger] e^{i\varphi_j}, \quad (23)$$

$$t_n = \delta_{n,0} + \frac{2}{\Omega_R} \lim_{T \rightarrow \infty} \frac{1}{T} \int_0^T dt e^{-i(\omega+n\Omega)t} \sum_{j=1}^N [\text{Tr} \rho(t) \sigma_j^\dagger] e^{-i\varphi_j}. \quad (24)$$

The calculated forward and backward scattering spectra $P_{\rightarrow} \equiv |t_n|^2$ and $P_{\leftarrow} \equiv |r_n|^2$ are shown in Fig. 6. In the limit of vanishing driving power this calculation yields the same results as the one presented in the main text. Namely, the $\alpha = \pi$ phase difference between the modulation tones of first and second qubits corresponds to strong inelastic backscattering, see Fig. 6d. Increase of the Rabi frequency leads to a gradual suppression of the scattering directionality that persists up to $\Omega \approx 3\Gamma_1$. This can be interpreted as a result of the saturation of the qubit transition induced by a strong driving [8].

SUPPLEMENTARY METHODS

Modulation amplitude calibration

The measured frequency dependence of the modulation amplitude $A_m(\Omega)$ is shown in Fig. 7a. It is caused by the various low pass filter stages we use to suppress external flux noise on the bias input line. To calibrate the modulation amplitude A_m we measure the transmission spectrum $|t_0|^2$ of a modulated qubit at the amplitudes A_V from 0 to 0.1 V_{pp} and for different modulation frequencies Ω .

For each value of Ω , we fit A_m as a linear function of A_V as shown in Fig. 7b. The linear fit is sufficient since we are far away from the flux sweet spot of the transmon qubit and $\partial^2 E_{01}/\partial\phi^2 \approx 0$. After repeating this procedure for each qubit separately where one is tuned to $\omega_0/(2\pi) = 6.129$ GHz and the other is far (> 2 GHz) detuned, we can now calculate the required A_V to result in the desired A_m for all Ω .

SUPPLEMENTARY FIGURES

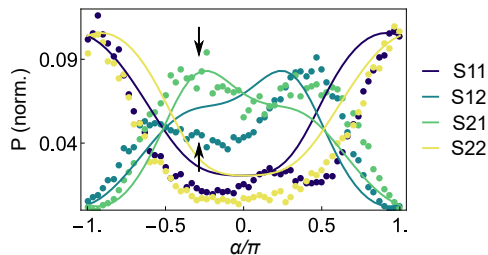


FIG. 5. **Isolator scattering matrix.** Measured coherent inelastic scattering power of the Stokes component is normalized to theory and shown as a function of the relative phase between modulation tones α at $(\omega - \omega_0)/(2\pi) = \Omega/(2\pi) = 20$ MHz.

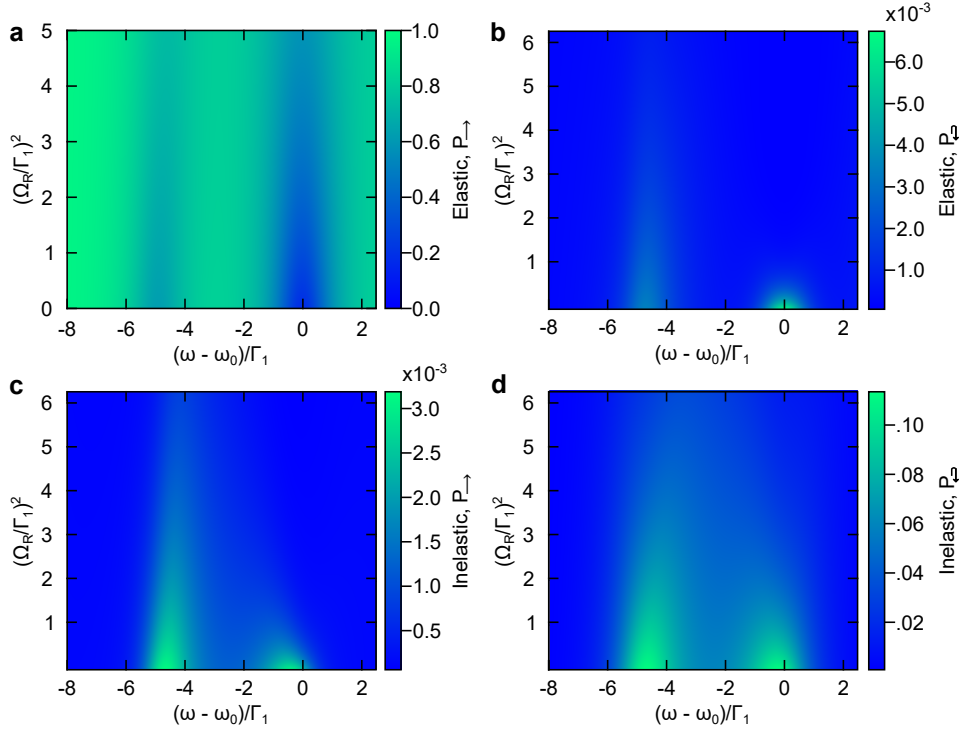


FIG. 6. **Dynamic range of directional scattering.** Calculated coherent elastic (a, b) and inelastic (c, d) scattering spectra as a function of normalized drive frequency $(\omega - \omega_0)/\Gamma_1$ and drive power $(\Omega_R/\Gamma_1)^2$ theoretically predicted for reflection (a, c) and transmission (b, d). The calculation has been performed for the modulation phase difference $\alpha_2 - \alpha_1 = \pi$ and $\Omega = A_m = 5\Gamma_1$.

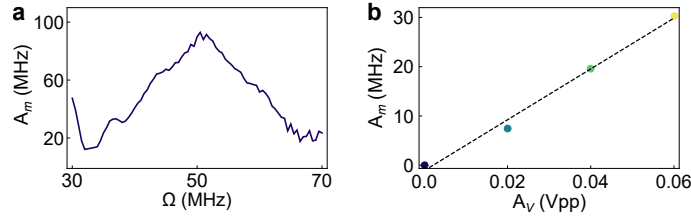


FIG. 7. **Modulation amplitude calibration.** a, Measured dependence of the modulation amplitude A_m on the modulation frequency Ω at the fixed AWG amplitude $A_V = 0.2 V_{pp}$. b, Measured dependence of the modulation amplitude A_m on the applied AWG amplitude A_V at the modulation frequency $\Omega = 20$ MHz.